Environmental Modelling and Software 193 (2025) 106645

Contents lists available at ScienceDirect

Environmental Modelling and Software

journal homepage: www.elsevier.com/locate/envsoft

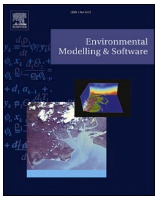

Uncertainty propagation analysis of remote sensing data in a coupled crop-radiative transfer model using particle filter and winding stairs

Amit Weinman [a,b], Raphael Linker [a], Offer Rozenstein [b,*]

[a] Faculty of Civil and Environmental Engineering, Technion – Israel Institute of Technology, Haifa, Israel
[b] Institute of Soil, Water and Environmental Sciences, Agricultural Research Organization – Volcani Institute, HaMaccabim Road 68, P.O.B 15159, Rishon LeZion 7528809, Israel

ARTICLE INFO

Keywords:
Crop model
Radiative transfer model
Coupled model
Remote sensing
Uncertainty propagation analysis
Winding stairs

ABSTRACT

Crop models can serve as decision-support tools, but their uncertainty must be accounted for. While previous research has shown effective calibration of crop models using remote sensing (RS) data, the remaining uncertainty is rarely quantified. This study investigated the propagation of errors associated with RS data in a coupled crop-radiative transfer model in two steps. First, the results of a Particle Filter (PF) process were examined to assess the uncertainty of the model parameters and outputs. Next, the Winding Stairs (WS) method was used to quantify the contribution of crop model parameters uncertainty to the total model uncertainty. The results show that parameters related to crop growth rate contribute more to the variance of simulated Leaf Area Index (LAI) and yield than the phenology-related parameters. These findings can guide future research to improve the model reliability by focusing on calibrating the parameters with a higher impact on model outcome uncertainty.

1. Introduction

The outputs of environmental models suffer from inherent uncertainty for various reasons, including simplifying complex environmental processes or errors in the model inputs (Chapagain et al., 2022). When such models are used as decision-support tools, these uncertainties must be reliably quantified to enable stakeholders and decision-makers to have a more comprehensive understanding of model predictions (Rosenzweig et al., 2013; White et al., 2016). This requirement is valid across several research fields, including climate, hydrology (Senatore et al., 2022), ecology (Walther et al., 2025), natural resources management (NRM) (Milner-Gulland and Shea, 2017), and agriculture (Correndo et al., 2021).

Within a modeling framework, three primary uncertainty sources can be identified. First is the uncertainty associated with the model structure imperfection, which stems from the gap between the real-life underlying environmental process and how the model simulates this process. This gap arises due to a limited understanding of the underlying process or a simplified description implemented in the model (Zheng et al., 2021). Second, the uncertainty is associated with the model inputs. In the current study, the terminology of Wallach and Thorburn (2017) is adopted, where model inputs include the external factors provided to the model. In environmental processes, these factors usually include weather data and management conditions (Uusitalo et al., 2015). The third uncertainty source is the model parameters. Models simulating complex systems may include tens or hundreds of parameters (Lin and Yang, 2022). Additionally, since not all parameters represent an actual physical value, they cannot all be evaluated by a direct measurement but must be calculated via model calibration. This procedure propagates the uncertainty of the observations to the parameters being assessed.

Two approaches have been adopted from inferential statistics for evaluating model parameters: the frequentist approach and the Bayesian approach (Ellison, 2004). In the frequentist approach, the parameters are assumed to have true, fixed values. Thus, they can be evaluated with a statistical procedure using the measured model state values without considering any knowledge regarding their prior values. Conversely, in the Bayesian approach, the parameters are considered random variables. They are evaluated by updating their prior distribution using measurements to obtain a posterior distribution. In Bayesian statistics, the concept of a confidence interval, which relies on frequentist interpretations of repeated sampling, does not apply. Instead, credible intervals are employed, representing the range within which a parameter lies with a specified posterior probability (Omlin and Reichert,

---

* Corresponding author.
E-mail address: offerr@volcani.agri.gov.il (O. Rozenstein).

https://doi.org/10.1016/j.envsoft.2025.106645
Received 8 April 2025; Received in revised form 16 June 2025; Accepted 3 August 2025

1999). Ghorbani et al. (2023) showed that the Bayesian approach was superior in evaluating model parameter values, especially in cases with sparse measurements and many parameters. Moreover, the Bayesian method is preferable to investigate model uncertainty as it expresses the model parameters and outputs as random variables characterized by a distribution (Ran et al., 2022). Furthermore, these posterior distributions can be utilized in error propagation analyses (Moges et al., 2020).

Since environmental models are usually complex and highly nonlinear, it is not plausible to evaluate the posterior distribution of their results in an analytical, deterministic fashion (King et al., 2023). Hence, numerical methods, such as Monte Carlo (MC) algorithms, are commonly applied. Applying MC algorithms in dynamic models includes sampling random sets of parameters from a proposed distribution and calculating the model results corresponding to these parameter sets (Omlin and Reichert, 1999). Several studies applied variations of the Markov Chain Monte Carlo (MCMC) method to quantify the uncertainty associated with model parameters in crop models (Alderman and Stanfill, 2017; Gao et al., 2021; Ran et al., 2022). MCMC methods are based on the basic Metropolis algorithm, where the posterior distribution is approximated by creating a chain of parameter values obtained by a random walk on which an acceptance/rejection rule is applied.

An alternative sampling method is the Particle Filter (PF), which has been shown to perform better than MCMC methods on dynamic models with many parameters and frequently available observations (Huang et al., 2019a). In a PF, the posterior distribution is represented by random samples called particles. The particle ensemble is created by sampling from the parameter space, propagated by running the model, and then assigned weights according to their fit with an observation (Orlova and Linker, 2023).

Aside from choosing the right method for uncertainty assessment, it is important to quantify the relative contributions of the different model elements to the overall uncertainty of the model output. This task can be performed by different sensitivity analysis procedures, such as ANOVA-based methods (Teixeira et al., 2017; Wallach et al., 2016). As an alternative, Jansen et al. (1994) introduced the Winding Stairs (WS) method, which is based on the Monte Carlo approach. An important feature of WS is that it can efficiently assess the uncertainty contribution not only of individual parameters but also of groups of parameters or inputs. Such an analysis was performed in the present study on a crop model.

Crop models simulate crop growth and development using mathematical equations describing the underlying bio-physical processes (Asseng et al., 2015). Crop model inputs include weather, soil attributes, and management conditions, which describe practices employed by the farmer, including irrigation, fertilization, and sowing and harvesting dates. The crop model parameters describe the distinct properties of a particular cultivar or variety and determine the duration of phenological stages, and parameters that directly affect the crop growth rate, such as photosynthesis rate or the ratio between biomass addition and leaf expansion rates. Variations in model structure consist of the growth-limiting factors (e.g., radiation or water availability) or using different equations for describing plant growth or soil-water interactions (de Wit et al., 2019).

Due to the complexity of cropping systems, crop models must be adapted to local conditions to simulate specific cases properly. This adaptation requires observed data, which is hard and tedious to measure in the field. Moreover, manually obtained measurements are point-specific and might not capture the spatial variance within a crop field. Hence, remote sensing (RS) measurements are widely adopted for data assimilation (DA) in crop models. RS data can help estimate the plant growing rate and health conditions in a non-destructive fashion (Weksler et al., 2022). Additionally, airborne or spaceborne RS data provides insights regarding the spatial variability of the measured property (Huang et al., 2019a). A difficulty arising from assimilating RS data into crop models is that crop models do not simulate the quantities captured by RS sensors, such as reflectance and radiance. This gap can be bridged by applying empirical relations between RS products (e.g., vegetation indices) and properties simulated by the crop model (e.g., Leaf Area Index (LAI), leaf nitrogen level) (Dlamini et al., 2023). Another option is to use radiative transfer models (RTM), simulating the interaction between the plant and soil and the solar radiation, to directly simulate the reflectance (e.g., Huang et al. (2019b)). This approach uses a subset of the crop model states to evaluate some of the RTM parameters at a specific time, enabling a direct comparison between the simulated and measured reflectance.

Despite its clear advantages, RS data suffers from measurement noise stemming from various factors, including sensor noise, atmospheric conditions, and simplifying assumptions (e.g., Lambertian reflectance) (Gorroño et al., 2017). This uncertainty is propagated into byproducts of RS measurements, such as vegetation indices (VIs) or retrieved crop traits (García-Haro et al., 2018; Graf et al., 2023). When these products are assimilated into a model, their uncertainty propagates to the predictions of the adjusted model.

Although it has been reported that uncertainties in assimilated RS data directly affect the predictions of the adjusted model (Jin et al., 2018; Rosenzweig et al., 2013), a rigorous investigation of uncertainty propagation in coupled crop growth-radiative transfer models has not been reported. Huang et al. (2019a) addressed the issue of assimilated observations' uncertainty and recommended using physical variables measured by the sensor (e.g., radiance, reflectance) rather than crop traits derived using intermediate processes such as RTM inversion. They argue that such intermediary steps require additional uncertainty propagation estimation. In a previous study, Zare et al. (2022) examined the propagation of the uncertainty of satellite observations to the uncertainty of crop model results utilizing a crop trait derived by an intermediate process. They calibrated the equation of the Choudhury model to relate the RS data to LAI and used the regression residuals to evaluate the uncertainty associated with the assimilated LAI. Next, they quantified uncertainties of simulated LAI and yield using a particle filter. In a different study, Levitan et al. (2019) used spaceborne observations obtained by the LANDSAT and MODIS satellites to calibrate a linear relation between the Enhanced Vegetation Index 2 (EVI2) and LAI. They assessed the confidence intervals of the linear regression coefficients with bootstrapping and used the values within these intervals to get a range of satellite-derived LAI values, which were compared to the LAI observed in the field or simulated by the crop model. While Zare et al. (2022) highlighted the reduction in the overall uncertainty of the model outputs due to DA in their conclusions, Levitan et al. (2019) noted that the uncertainty in the relationship between satellite observations and crop model states stemming from site and growth-stage specific factors is significant and substantially impairs the crop model calibration results.

This paper investigates the propagation of reflectance uncertainties to the parameters and predictions of a coupled crop-radiative transfer model (Weinman et al., 2025a). The innovative aspect of this study is twofold. First, it presents a novel use of parameter distributions derived from a particular set of measurements to quantify uncertainty propagation in a coupled crop-radiative-transfer model. This analysis produces the uncertainty associated with the coupled model outputs and the relative contribution of different crop model parameter types to the outputs' overall uncertainty. According to Chapagain et al. (2022), understanding the contribution of the observation uncertainty to the model uncertainty is still lacking, and no previous study has implemented uncertainty analyses in crop modeling on processing tomatoes, which is the crop used in the present study. Second, in this paper, the assimilated measurement is canopy multispectral reflectance rather than one of the byproducts that can be obtained by post-processing (e.g., reflectance-derived LAI). This approach enables the overcoming of limitations arising from the inadequate assessment of the uncertainty introduced by the intermediate processes (Huang et al., 2024).

2. Methods

2.1. *Experiments*

The suggested uncertainty propagation framework was applied to processing tomatoes using synthetic and real-life data. Using synthetic data reduces the uncertainties associated with the model structure, parameters, and inputs, thus enabling focus on the effect of the observation noise on parameter calibration and the associated uncertainty. On the other hand, the real-life experiment demonstrates the effect of the additional uncertainty sources on the framework's performance and its applicability in the real world.

2.1.1. *Real-life experiment*

The real-life data was obtained from a field experiment spanning an entire growing season of processing tomatoes of cultivar H4017. The experiment was conducted in the Hulla Valley, located in the north of Israel, in Gadash Farm ($33^\circ 10' 54'' N, 35^\circ 34' 47'' E$) in 2019. The experiment location is presented in Fig. 1. Processing tomatoes were transplanted on 13 April and harvested on 30 July. The crop was drip-fertigated throughout the season. The weather during the growing season was characterized by high temperatures during the daytime, very low precipitation, and low cloudiness. The soil in the field area is composed of alluvial brown Gromosols with a clay loam texture (Dan and Raz, 1970). Weather records were obtained from a meteorological station situated on the farm, and soil properties of the field were obtained by collecting soil samples from several depths and analyzing their particle size distribution and bulk densities. The particle size distribution analysis, conducted using laser diffraction, confirmed that the soil texture is clay loam. The particle size distribution was used to extract the soil hydraulic properties using DSSAT's SBUILD tool, which applies pedotransfer functions (Wilkens et al., 2010).

LAI was measured on the following days after planting (DAPs): 33, 45, 60, 75, 88, and 103, using a SunScan Canopy Analysis System SS1 (Delta-R, Cambridge, UK). A single LAI measurement included 30 SunScan readings taken at even intervals between the centers of three adjacent crop rows with the device probe directed in parallel to the row's direction. The SunScan system evaluates LAI based on the difference in solar radiance measured above and below the plant canopy (Kaplan et al., 2021). The total yield, as well as irrigation and fertilization schedules, were provided by the farmer. The produced yield (6.5×10^4 kg/ha) was relatively low compared to the regional average (approximately 10×10^4 kg/ha). This poor yield might stem from the extensive weed spread observed in the field, including Egyptian Broomrape (*Orobanche aegyptiaca*).

For simulating the real-life case study with DSSAT-CROPGRO, the potential evapotranspiration (ET_0) was calculated using the Ritchie modification of the Priestley-Taylor method (Boote et al., 2008), as this method was found to represent best the effect of plant water status on crop growth for processing tomatoes in the local environmental conditions (Weinman et al., 2025b). The photosynthesis was calculated using the 'leaf photosynthesis response curve' method since this method describes photosynthesis more elaborately than the other available methods.

2.1.2. *Synthetic experiment*

The synthetic experiment consisted of running a model with prescribed parameters and input values, and the results of these runs were then considered virtual measurements used as the ground truth for further analysis performed with this model. Moreover, different levels of user-defined noise were added to the simulated results to mimic measurement uncertainty. The reason for employing this practice is to eliminate the uncertainties related to the model structure, inputs, parameters, and the noise of the measurements used for assimilation (Jamal and Linker, 2020; Orlova and Linker, 2023). Thus, in the present case, the synthetic experiment enabled focusing on the propagation of the predefined measurement noise through the DA scheme (Omlin and Reichert, 1999).

The case study implemented in the present synthetic experiment was similar to the real-life experiment (Section 2.1.1) in terms of weather, soil, and management conditions. The crop parameter values used to run the synthetic simulation are presented in Tables A1 and A2. The synthetic experiment differed from the real-life experiment with regard to the measurements used in the DA procedure; in the real-life case, the assimilated measurements were the Sentinel-2 observations detailed in Section 2.2. In contrast, in the synthetic experiment, the assimilated data was the reflectance results from running the coupled crop-radiative-transfer model. For consistency, the assimilated reflectance in the

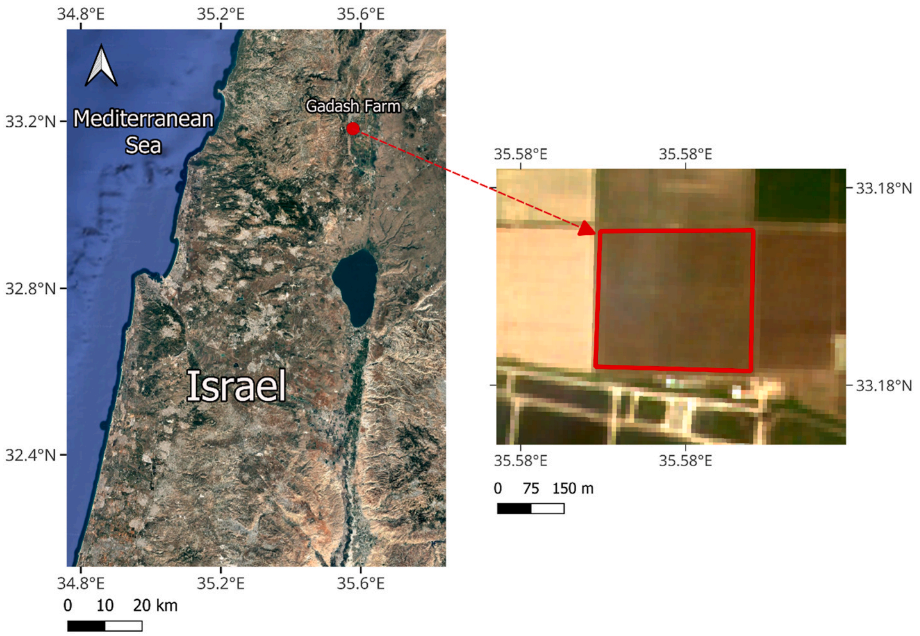

Fig. 1. Location of the processing tomato field from which real-life data was used. The red frame in the blow-up marks the research area. Base map sources: Google satellite (Map of Israel) and Sentinel-2 (blow-up map).

synthetic case was resampled according to the Sentinel-2 spectral response function, and the assimilation times corresponded to the dates Sentinel-2 images were available during the 2019 season. The synthetic experiment was run three times with different measurement noise levels (noise level estimated from the observations, 5 times lower, and 5 times higher than the observed noise) to investigate the effect of the measurement noise magnitude on the uncertainty propagation.

2.2. Remote sensing data

Remotely sensed data in this study consists of Sentinel-2 products. Sentinel-2 Earth observation mission is part of the European Space Agency (ESA) Copernicus program and consists of two polar-orbiting satellites, Sentinel-2A and Sentinel-2B. The revisit frequency of the combined satellite constellation is five days. Each satellite carries a Multispectral Instrument (MSI), with band wavelengths ranging from the RGB to SWIR domains. Table B1 summarizes the Sentinel-2 bands relevant to investigating vegetation traits and their spatial resolutions. Sentinel-2 level-2A data was obtained from the ESA Copernicus Open Access Hub website (Kaplan et al., 2021; Weiss and Baret, 2016). Sentinel-2 images were filtered based on two criteria: (a) clouds covering the experimental field, (b) manual inspection focusing on unreasonable behavior of the reflectance spectrum (e.g., reflectance at 664 nm (red) higher than at 559 nm (green) when the canopy was fully developed). During the 2019 season, there were 12 dates with available images of sufficient quality on DAPs: 13, 18, 28, 33, 38, 43, 58, 83, 93, 98, 103, and 108. The average of all the pixels within the experimental field (a total of 203 pixels) was used as measured reflectance, and the noise was set equal to the standard deviation of these pixels. This noise was used as the standard uncertainty level in the synthetic and real-life experiments (following Machwitz et al. (2014)).

2.3. Models

2.3.1. DSSAT-CROPGRO-tomato

The Decision Support System of Agrotechnology Transfer (DSSAT) is a collection of mechanistic crop growth models that interact with modules simulating processes like soil water balance, weather, and crop management to simulate crop growth and phenological development at a daily timestep (Jones et al., 2003). CROPGRO, a component of DSSAT, is a versatile model capable of simulating various crop types, including legumes, forage, and vegetables. It uses predefined phenology stages to account for plant development, which progresses based on accumulated growing degree days and photoperiods. Biomass accumulation in CROPGRO is influenced by weather conditions, particularly solar radiation, and is limited by abiotic stress from environmental and management factors. The current phenology stage determines how accumulated biomass is distributed among plant organs (Bosi et al., 2020; Cammarano et al., 2020). Scholberg et al. (1997) adapted CROPGRO to create the DSSAT-CROPGRO-Tomato model, incorporating a photosynthesis production rate equation originally developed for greenhouse tomatoes (Jones et al., 1991).

2.3.2. RTMo SCOPE

The Soil Canopy Observation of Photosynthesis and Energy fluxes (SCOPE) model (Yang et al., 2020) simulates the interaction between incoming solar radiation and vegetated surfaces, combining radiative transfer and energy balance principles. The focus of this study was on the RTM for incident radiation from the sun and the sky (RTMo) module, which calculates top-of-canopy outgoing radiation in the 0.4 to 2.5 μm spectral range. RTMo applies the Fluspect model, an extended version of the PROSPECT model (Jacquemoud and Baret, 1990), which calculates transmittance and reflectance at the leaf scale (van der Tol et al., 2016), the SAIL model (Verhoef, 1984), which accounts for canopy structure effects, and the Brightness-Shape-Moisture (BSM) model (Verhoef et al., 2018), which simulates the soil reflectance. SCOPE version 2.0 was used in the present study while maintaining default values for all the parameters that were not explicitly updated through model coupling.

2.3.3. DSSAT-RTMo coupling

The coupling relations used in this study are detailed in Weinman et al. (2025a). A summary of the relations is presented in Table 1. In the real-life case, the BSM parameters 'brightness', 'Latitude', and 'Longitude' were calibrated based on a Sentinel-2 image of the field by the beginning of the season before planting (Yang et al., 2019). During this calibration, the SMC (soil moisture content) parameter was evaluated by the soil water content simulated by a CROPGRO run that started several months before image acquisition, thus accounting for the weather conditions before planting. For the rest of the season, the SMC parameter was updated according to the soil moisture simulated by DSSAT-CROPGRO, while the rest of the BSM parameters were kept constant at their values calibrated at the beginning of the season. However, throughout most of the season, the soil background had minimal impact on the simulated reflectance due to the tomato plants' ground coverage and the limited spatial resolution of Sentinel-2 level-2A reflectance images, which do not enable the separation of pixels that contain only soil or vegetation.

2.4. Particle filter

The particle filter (PF) procedure implemented in this study is adopted from Weinman et al. (2025a), with several modifications applied to enhance PF performance when using real-life instead of

Table 1
– Summary of the parameters included in the coupling scheme.

SCOPE RTMo parameters		DSSAT-CROPGRO parameters		Source
Name	Description	Name	Description	
Leaf parameters				
$\boldsymbol{C_{ab}}$ $[\boldsymbol{\mu g / cm^2}]$	Chlorophyll *a and b* content	LN%D, P#AD, SLAD	Nitrogen content, pod number, SLA	Guler and Buyuk (2007); Jiang et al. (2017)
$\boldsymbol{C_{ca}}$ $[\boldsymbol{\mu g / cm^2}]$	Carotenoid content			Ntakos et al. (2024)
$\boldsymbol{C_{dm}}$ $[\boldsymbol{g / cm^2}]$	Dry matter content	SLAD	Specific leaf area	Machwitz et al. (2014)
$\boldsymbol{C_w}$ $[\boldsymbol{cm}]$	Leaf water equivalent layer			Based on measurements (Weinman et al., 2025a)
$\boldsymbol{N}$ $[-]$	Leaf structure parameter			Jacquemoud and Baret (1990)
$\boldsymbol{C_s}$ $[-]$	Senescent material fraction	L#SD	Leaf number per stem	Jones et al. (2010)
Canopy parameters				
LAI $[-]$	Leaf area index	LAID	Leaf area index	Machwitz et al. (2014)
$\boldsymbol{LIDFa}, \boldsymbol{LIDFb}$ $[-]$	Leaf inclination distribution parameters	GSTD	Growth stage	Based on measurements (Weinman et al., 2025a)
Soil reflectance				
BSM (Brightness, Latitude, Longitude)	Model for soil reflectance	Calibrated according to a Sentinel-2 image captured by the beginning of the season before planting. (Yang et al., 2019)		
SMC	Soil moisture content	SW1D	Soil water content in the upper soil layers (depth range of 0–5 [cm])	Yang et al. (2019)

synthetic data. This PF procedure is based on Orlova and Linker (2023), who presented a sensitivity-based PF algorithm. The following section briefly describes the PF, while the reader is referred to the two aforementioned studies for more details.

The PF algorithm began by creating a sample of CROPGRO parameter values. Hereafter, adopting the commonly accepted terminology, a single sample element is called a particle, while the whole set of sample elements is called an ensemble. The values of the parameters were sampled from a uniform distribution with boundaries set according to a literature review (Xu et al., 2021) (See Table A1). The sampling method for creating the initial particle ensemble was Latin-Hypercube (Van Griensven et al., 2006). Next, whenever an observation was introduced, the particles were reassigned with weights according to the fit between their predictions and the observation. The weights were determined using a Gaussian distribution:

$$w_{i,b}^{t}=\frac{1}{\sigma_{b}^{t}\sqrt{2\pi}}\exp\left(\frac{-\left(\nu_{i,b}^{t}-\mu_{b}^{t}\right)^{2}}{2\left(\sigma_{b}^{t}\right)^{2}}\right) \tag{1}$$

where the superscript t refers to the time step and the subscript i refers to the i-th particle. ν is the simulated reflectance, and μ and σ are the corresponding mean and standard deviation of the measurement. The subscript b refers to a specific band.

After computing the weights for each band and each particle, the weights of all bands for a specific particle were summed up:

$$w_{i,b\_sum}^{t}=\sum_{b=1}^{N_b} w_{i,b}^{t} \tag{2}$$

where, N_b is the number of bands.

Next, the weight of each particle w_i^t was obtained by normalizing w_{i,b_sum}^{t} by their sum:

$$w_{i}^{t}=\frac{w_{i,b\_sum}^{t}}{\sum_{i=1}^{N_p} w_{i,b\_sum}^{t}} \tag{3}$$

where N_p is the number of particles in the ensemble. Once the particle weights had been calculated, the ensemble weighted average was calculated according to:

$$E(y^t)=\sum_{i=1}^{N_p} w_i^t y^t \tag{4}$$

where y^t stands for the measure of interest (reflectance, LAI, or yield) at time t.

Before performing the next DA step at the next available observation date, the ensemble was updated using sensitivity analysis results. The SA procedure and its results are detailed in Weinman et al. (2025a). The ensemble update included a resampling step applying the stochastic universal resampling method (Van Leeuwen, 2009). This step aims to prevent filter degeneracy by replacing particles with low weights with particles with high weights. Next, each particle was modified with random noise by perturbing the four parameters to which the simulated reflectance was most sensitive at the current time step. The perturbation was performed by adding Gaussian noise with zero mean and standard deviation determined by the parameter value and a predefined tuning factor (Orlova and Linker, 2023), according to:

$$\alpha_i^{t+1}=\alpha_i^t+\eta_i \quad where\ \ \eta_i\sim N\left(0,\varepsilon_p\alpha_i^t\right) \tag{5}$$

where, α is the parameter value, η is the added noise, and ε_p is the tuning factor. The ε_p value used here is 0.08, as in Weinman et al. (2025a).

2.5. Winding stairs

The following section briefly portrays the winding stairs (WS) method and its adaption to the current study. For a more comprehensive description of WS, see Jansen et al. (1994) and Chan et al. (2000). Jansen et al. (1994) introduced WS as a sampling method for distinguishing the contributions of different uncertainty sources of a model to the model's total uncertainty. To formalize this analysis, the model output can be described as a function of two input random variables, U and V, which represent independent uncertainty sources. A function representing the model, f, can be formulated as follows:

$$f(u,v)=f_0+f_u(u)+f_v(v)+f_{uv}(u,v) \tag{6}$$

where, u and v are possible realizations of U and V, f_0 is the best estimate of f when U and V are unknown, $f_u(u)$ and $f_v(v)$ are the correction when only U or V, respectively, become fully known, and $f_{uv}(u,v)$ is the remaining difference between f and f_0. $f_u(u)$ and $f_v(v)$ are called the main effects of U and V, respectively, and $f_{uv}(u,v)$ is called the interaction of u and v. Next, the overall variance of the model can be presented as:

$$Var(f(U,V))=Var(f_u(U))+Var(f_v(V))+Var\left(f_{u,v}(U,V)\right) \tag{7}$$

The terms in Eq. (7) are used by Jansen et al. (1994) to evaluate two variance metrics corresponding to each of the uncertainty sources, namely the top marginal variance (TMV) and the bottom marginal variance (BMV). TMV from U is defined as the expected reduction in the variance of $f(U,V)$ if U should become fully known, while V remains unknown. Accordingly, TMV from U equals $Var(f_u(U))$. On the other hand, BMV from U is defined as the expected remaining variance of f if V should become fully known, while U remains unknown, which equals $Var(f_u(U))+\ Var\left(f_{u,v}(U,\ V)\right)$. It follows that if there is no interaction between the uncertainty sources, BMV equals TMV.

The WS sampling method aims to assess the contribution of each uncertainty source separately. Unlike regular MC methods, where a new model realization is obtained after sampling from all the variance contributors, in WS, f is calculated after sampling from a single uncertainty source each time. The method is illustrated by a matrix containing the model realizations, where each row comprises a sequence of model realizations that include sampling from all the uncertainty sources. Each such row is called a *cycle* (Chan et al., 2000; Jansen et al., 1994). To demonstrate this concept, let q represent the output of a model f (e.g., yield or LAI) with two uncertainty sources M_1 and M_2.

$$q=f(M_1,M_2) \tag{8}$$

The corresponding sampling matrix, with four cycles, is:

$$\begin{bmatrix} q_1 & q_2 \\ q_3 & q_4 \\ q_5 & q_6 \\ q_7 & q_8 \end{bmatrix}=\begin{bmatrix} f(M_{11},M_{21}) & f(M_{11},M_{22}) \\ f(M_{12},M_{22}) & f(M_{12},M_{23}) \\ f(M_{13},M_{23}) & f(M_{13},M_{24}) \\ f(M_{14},M_{24}) & f(M_{14},M_{25}) \end{bmatrix} \tag{9}$$

where, M_{ij} is the j-th randomly drawn sample of the values of the uncertainty source i. Since each element on a single column in Eq. (9) has unique sampling values, it can be assumed that all the corresponding model realizations are independent. Hence, the total variance in the output, $Var(q)$, can be calculated from each column.

Following, BMV from M_2 can be calculated according to:

$$BMV(M_2)=0.5^*Var(col1-col2) \tag{10}$$

Next, TMV from M_2 can be evaluated according to,

$$TMV(M_2)=Var(q)-0.5^*Var(col2-shift(col1)) \tag{11}$$

Where $shift(col1)$ indicates the first column shifted one step down.

In this study, the number of WS cycles found necessary to represent the model variance adequately was 10,000. The adequacy of the variance estimation was established based on two conditions: (1) the BMV values were higher than the TMV values for LAI throughout the season and for yield, as expected according to their definitions (Jansen et al., 1994), and (2) the variances calculated from both matrix columns (Eq. (9)) differed by 0.35 % for the final yield and by less than 2.15 % for the LAI.

2.6. Study description and workflow

The following section portrays the framework by which the PF and WS algorithms were used to analyze the propagation of assimilated RS data to model parameters and outputs. The framework is illustrated schematically in Fig. 2.

First, the measured data and its uncertainty were obtained, and the simulation details, including input and initial parameter values, were set. Next, the particle filter procedure was applied, resulting in particle ensembles describing the distributions of the CROPGRO parameters and variables of interest. The ensemble obtained after the resampling step of the last DA event and before the noise addition step was considered the model's final results. These results are presented in Section 3.1.

The WS analysis evaluated the contribution of two distinct subsets of CROPGRO parameters to the total output uncertainty. During the sampling step of the WS algorithm (for assembling the matrix in Eq. (9)), parameter values were sampled from the distributions obtained by the PF. In terms of the formulation presented in Eq. (8), M_1 corresponds to a subset of CROPGRO parameters determining phenology (EM-FL, FL-SD, SD-PM, and EM-V1), and M_2 corresponds to a subset of CROPGRO parameters that affect crop growing rate (CSDL, FMAX, SLAVR, XFRT, and TRIFL). These parameters were chosen since they were most influential on yield, LAI, and reflectance based on a global sensitivity analysis by Weinman et al. (2025a).

2.7. Performance evaluation metrics

To evaluate the distribution spread of the parameters evaluated during the PF run, the ratio between the distribution standard deviation and the predefined range of each parameter value was calculated. This metric was chosen since it allows for the comparison of different parameters with different nominal values and ranges and will henceforth be called the STD (standard deviation)-range ratio.

For reflectance, the nine Sentinel-2 bands presented in Table B1 were considered during RMSE calculation for each time step. For the synthetic case study, The RTMo output, whose spectral resolution is 1 nm, was resampled according to the Sentinel-2 spectral response function, and only the resampled values were used:

$$RMSE_{reflectance} = \sqrt{\frac{\sum_{b=1}^{N_b} (r_b - \widehat{r}_b)^2}{N_b}} \tag{12}$$

where, b stands for the spectral band, N_b stands for the total number of spectral bands, r stands for the observed reflectance, and $\widehat{r}$ stands for the simulated reflectance.

For LAI, RMSE of the seasonal LAI was evaluated considering six LAI measurements taken during the season (for both the real-life and synthetic case study):

$$RMSE_{LAI} = \sqrt{\frac{\sum_{k=1}^{N_k} (y_k - \widehat{y}_k)^2}{N_k}} \tag{13}$$

where, k stands for the date of measurement, N_k stands for the total number of measurements during the season, y is the observed LAI data, and $\widehat{y}$ stands for the simulated results.

For the final yield, the Normalized Absolute Error (NAE) was used:

$$NAE = \frac{|yield_{obs} - yield_{simulated}|}{yield_{obs}} \times 100 \tag{14}$$

The uncertainty of the coupled model output was quantified using the 50 % and 90 % Credible Intervals (CI), as suggested by Wallach et al. (2012). A CI with a certain probability is used under the Bayesian approach to define the interval that contains the model results with this probability according to the current state of knowledge (Omlin and Reichert, 1999). CIs were calculated according to the definition that the range of a $1 - \alpha$ credible interval is limited by the $\alpha/2$ and the $1 - \alpha/2$ quantiles (Omlin and Reichert, 1999).

3. Results

3.1. Uncertainty assessment through PF simulation

Fig. 3 shows the distributions of the parameters adjusted during the particle filter run, obtained after the resampling step of the final DA step. The red line shows a normal density function fitted with MATLAB's *histfit* function (version R2023b), which uses the maximum likelihood estimation method. The number in the top-left corner of each subplot is

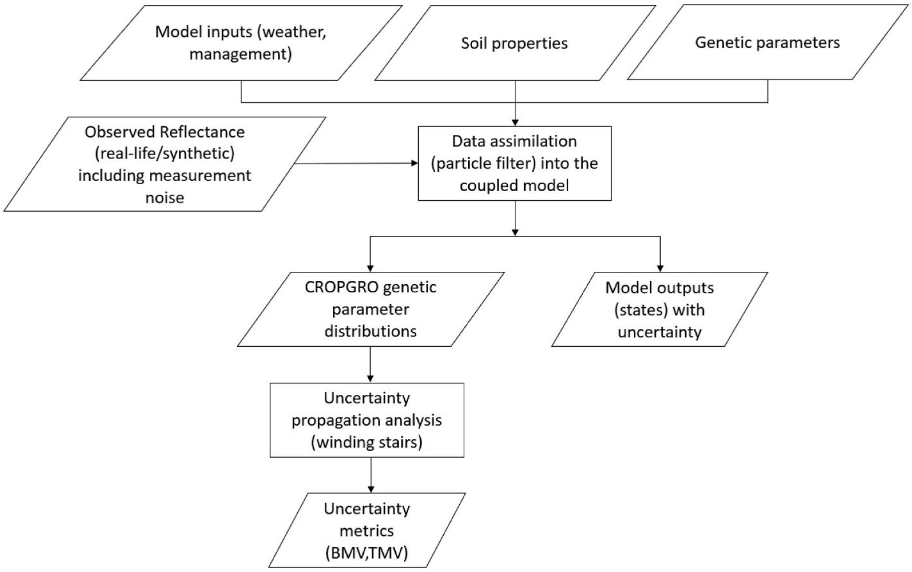

Fig. 2. Schematic illustration of the uncertainty propagation workflowe

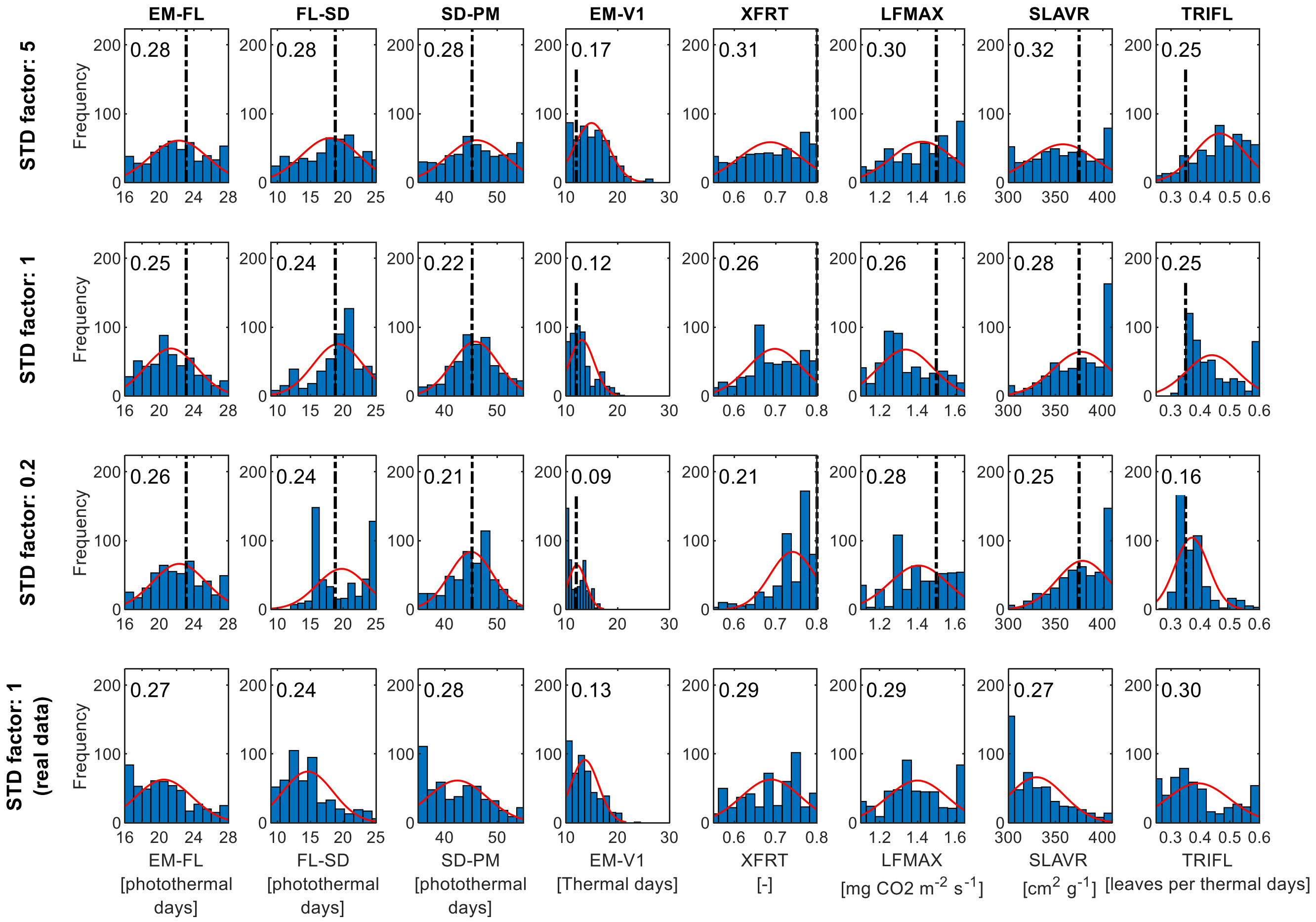

Fig. 3. – Distributions of the adjusted parameters after the final data assimilation step. The top three rows show the distributions obtained in the synthetic experiments, with the vertical dashed line indicating the true parameter values. An STD factor of one indicates that the STD assigned to the synthetic reflectance was equal to the observed one. STD factors of 0.2 and five indicate that the assigned STD was the one from observation multiplied by 0.2 and five, respectively. The bottom row presents the results from the real-life case. The red line shows the fitted normal density function. The number presented in the top-left corner of each subplot is the ratio between the standard deviation and the predefined range of each parameter. Each column corresponds to a specific parameter, identified by its DSSAT acronym.

the STD-range ratio described in Section 2.7.

For the synthetic case, Fig. 3 shows that the convergence of SLAVR and TRIFL toward their baseline values improved as the STD factor decreased, whereas the convergence of LFMAX and XFRT did not show such a trend. XFRT converged poorly due to its low impact on LAI and reflectance during most of the season, which led to its perturbation only at the final DA step (details not shown). The fact that SLAVR converged well while LFMAX did not, although increasing both these parameters generally increases LAI, might be explained by the impact of SLAVR on RTMo parameters C_{dm} and C_w, through the SLAD (daily specific leaf area) state, as formulated in the model coupling scheme (section 2.3.3).

Fig. 3 presents a general decrease in the STD-range ratio of each parameter with decreasing noise values, indicating that, as expected, noisier measurements tend to result in more uncertain parameter values. The only exceptions are the parameters EM-FL and LFMAX, for which the spread of the parameters was higher for the lowest noise, and TRIFL, where the spread was reduced only for the lowest noise value. The relatively high STD-range ratio values of LFMAX and SLAVR at the lowest noise level can be explained by the fact that LAI, an essential factor in determining the simulated reflectance, is equally sensitive to these two parameters. The phenology parameters tended to converge with lower spreads compared to the growth rate parameters, with the parameter EM-V1 showing the lowest STD-range ratio for all noise levels. The distributions for the real-life case showed trends comparable to the synthetic cases with STD factors 1 and 5. In particular, lower value spreads were obtained for the phenology parameters than for the growth rate parameters, with the lowest spread for EM-V1.

Fig. 4 shows the reflectance results obtained during the particle filter run for the synthetic experiment with the three noise levels (three left columns) and the real-life case with the measured noise (right column). For brevity, only the results obtained at three DA steps corresponding to the beginning, middle, and end of the season are presented.

Examining the results of the synthetic case, the RMSE of the case with an STD factor of 5 at DAP 108 was three times higher than the second-worst RMSE. This gap might result from the cumulative effect of the larger noise as more DA steps were executed, which led to poor convergence of the particle filter. The larger divergence for the highest noise was also expressed by the larger spread of the particles. For the synthetic case with an STD factor of 1 at DAP 108, the simulated spectra are separated into two clusters that differ in terms of reflectance values at wavelengths higher than 740 nm. This separation stemmed from the particles having different values of the phenology-related parameters. This difference led to different growing stages at DAP 108, which affected the LIDF values according to the coupling scheme (section 2.3.3). For the case with an STD factor of 5, these two clusters were closer to one another due to the larger spread of the spectra.

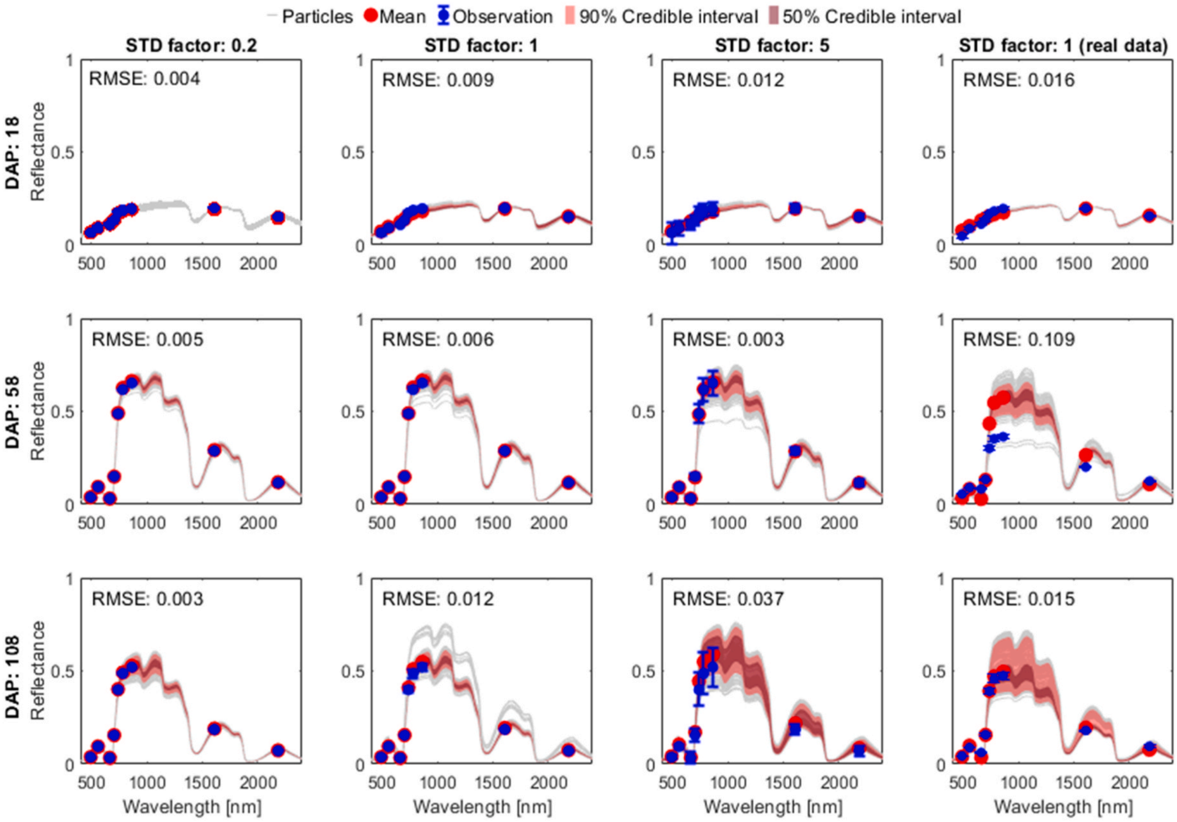

Fig. 4. – Reflectance results of the particle filter for synthetic cases with three noise levels and the real-life case. The grey curves represent the particles, the red markers indicate the weighted mean of the estimated reflectance at the bands of Sentinel-2, after applying the Sentinel-2 spectral response function, and the blue markers represent the observed data, with the error bars indicating measurement noise. The light and dark red intervals represent the 90% and 50% credible intervals (CI), respectively. Each row of subplots corresponds to a date on which DA was performed. The three leftmost columns present the synthetic cases with different noise levels while the right column presents the real-life case.

Fig. 4 shows that for the real-life case, the fit between the measured and simulated spectra at the beginning and the middle of the season was poorer than in the synthetic case (regardless of the noise level used). At DAP 58, the RMSE of the real-life case was distinctively high, reaching 0.109. In this case, the simulated reflectance corresponded to a fully developed, healthy canopy, whereas the measurements were consistent with a less developed canopy. This trend is indicated by the simulation showing higher reflectance values at 704, 740, and 782 nm (red-edge and NIR bands) and lower reflectance values at 492 and 664 nm (blue and red bands). Since the fit between simulated and measured LAI at this DA step was acceptable (see fit at DAP 58 in the corresponding panel in Fig. 5), the discrepancy in reflectance must be explained by a misfit of the other coupling relations. For example, an erroneous relation between the crop growing stage and the leaf inclination angle distribution, which is represented by the LIDF parameter. Nonetheless, for the real-life case at DAP 108, the reflectance RMSE was similar to the synthetic case with the observed noise, and in both cases, the measurements were within the 50 % CI.

The three leftmost columns in Fig. 5 show the effect of the measurement noise level on the LAI RMSE for the synthetic cases. This effect is most pronounced on the last DA step at DAP 108, where the RMSE of the case with an STD factor of 0.2 was lower by 0.99 than the case with an STD factor of 5. The difference in the noise level was also expressed in the spread of the 90% and 50% CIs. Comparing the synthetic cases with STD factors of 1 and 0.2, the magnitudes of the CIs, which indicate the simulation uncertainty level, were quite similar. However, the observation was not within the 50 % CI in the case with an STD factor of 1 from DAP 50.

Compared to the synthetic case, the PF in the real-life case (rightmost column in Fig. 5) showed a more pronounced improvement, with an RMSE reduction of 1.1 and a notable narrowing of the 50% CI. The RMSE of the real-life case was between the RMSE values of the synthetic cases with STD factors 1 and 5. Unlike these two synthetic cases, where the measured LAI was within the 50% CI only at the beginning of the season, in the real-life case, the observations at DAPs 33, 60, 75, and 103 were within the 50% CI, while the observations from DAPs 45, and 88 were not. This trend points out an inconsistency in the LAI measurements that probably stemmed from flaws in the measurement process. Such measurement inconsistencies lead to a reduction in RMSE, which cannot be corrected by improving the modelling or the DA frameworks.

Fig. 6 presents the final yield results, including histograms that show additional information regarding the spread of the ensemble predictions. Considering the results of the synthetic experiment, it is surprising that the results obtained at DAP 108 do not show a trend between the noise level and the NAE value or the magnitude of the CIs. That is, the RMSE in the case with the lowest noise was higher than the other synthetic cases, and its 50% CI spread was larger. These results do not align with the reflectance and LAI results presented in Figs. 4 and 5, where the lowest measurement noise led to the best RMSE and CI values. Examining the real-life case, the yield was predicted extremely well at DAP 108, but the 50 % CI values were larger than in the synthetic cases. The histograms in Fig. 6 show that the final yield estimates at DAP 108 for the synthetic cases with STD factors of 1 and 0.2 were not normally distributed. This finding indicates that not all particles that simulated reflectance well (and hence achieved high weights) also predicted yield accurately. This trend demonstrates the equifinality problem of the crop model, where different sets of parameters might yield similar simulated reflectance but different simulated yields.

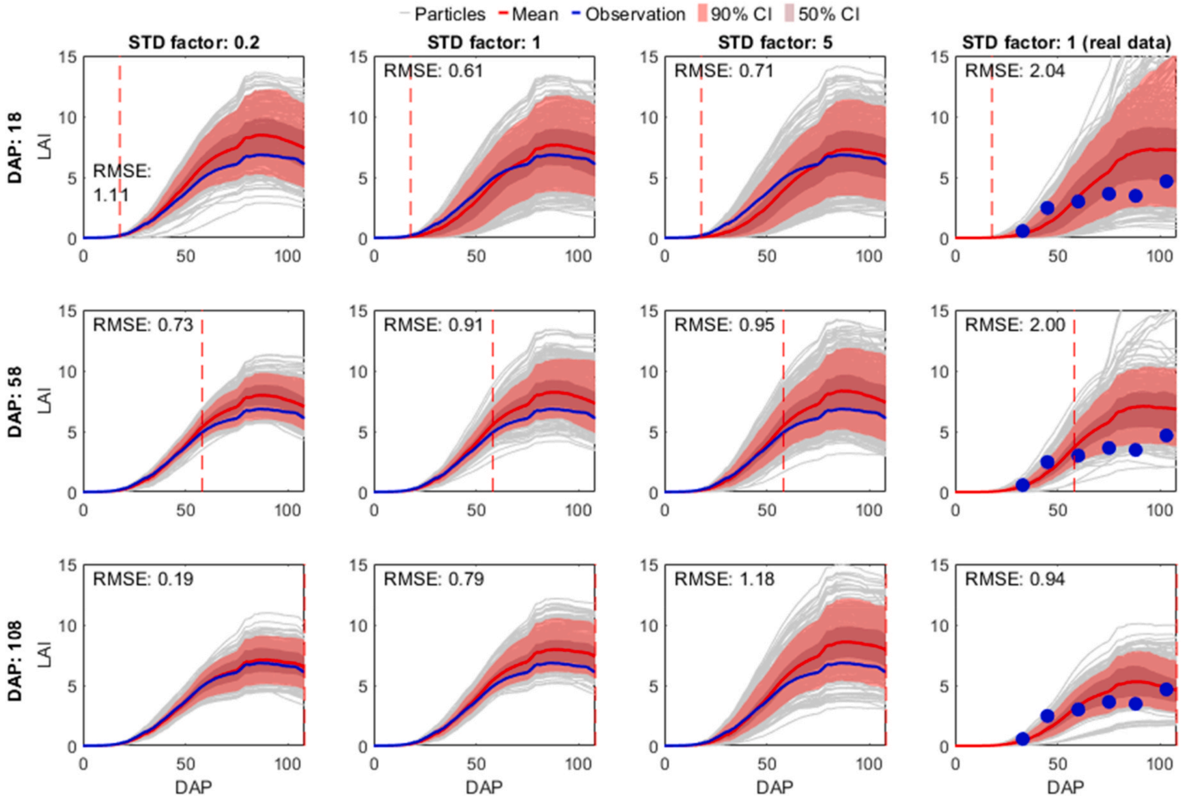

Fig. 5. – LAI results of the particle filter for synthetic cases with three noise levels and the real-life case. The grey curves represent the particles, and the red curves and markers indicate the weighted mean of the LAI for the synthetic and real-life cases, respectively. The blue curves and markers represent the observed LAI for the synthetic and real-life cases, respectively. The light and dark red intervals represent the 90% and 50% credible intervals (CI), respectively. The RMSE presented on the top-left corner of each subplot was calculated only for the LAI values at the six dates when LAI measurements were available, as indicated in the right column. Each row of subplots corresponds to a date on which DA was performed. The three leftmost columns present the synthetic cases with different noise levels while the right column presents the real-life case.

3.2. *Winding stairs results*

The results of the uncertainty propagation through WS analysis are presented only by the bottom marginal variance (BMV) values since the differences between BMV and TMV for a particular uncertainty source were not substantial for any of the cases investigated. These minor differences indicate that the variance contributed by the interaction between the two uncertainty factors is very small. Thus, the sum of the BMV values of the two sources equals the total variance. In the following figures, the total variance is separated into the contributions of the phenology (blue curve) and the growth rate (orange curve) parameters.

Fig. 7 shows that in the synthetic cases, the total variance value changed almost linearly with respect to the noise magnitude at the values examined in this analysis. For all cases, the BMV of the growth rate parameters increases until approximately DAP 90, when it starts to decrease. The phenology parameters' BMV is monotonically increasing with different curves along the season. This trend can be explained by the fact that the duration of a single phenological stage (e.g., from emergence to flowering) affects the rest of the season since phenology stages are sequential, and thus, their impact is cumulative. On the other hand, the effect of the growth rate parameters decreases when the plant reaches senescence, and LAI starts declining due to biomass allocation to the reproductive organs. For the synthetic cases, the increase in the STD factor affects the BMV of the growth rate to a greater extent than the phonology parameters, meaning that these parameters contribute more to the total variance as the noise level increases.

Fig. 8 shows the BMV values of the yield. For the synthetic cases, the total variance decreased approximately linearly with the decrease of the noise magnitude at the values examined in this analysis. Overall, decreasing the noise level times 10 reduced the total BMV by almost a factor of 2 (from $4.23*10^8$ to $2.38*10^8$ [$(kg/ha)^2$]). In contrast, the BMV contributed by the phenology parameters decreased more rapidly between the cases with STD factors of five and one than for STD factors of one and 0.2. The real-life case had a total variance value equal to the synthetic case with an STD factor of five, but the BMV of the phenology parameters was similar to that observed with the 0.2 STD factor. The findings presented in Figs. 7 and 8 suggest that the additional uncertainty in the real-life case, associated with the uncertainty in model structure and inputs, led to a worse convergence of DSSAT parameters during the DA procedure than for the synthetic case with the same measurement noise. This difference is mainly pronounced for the growth rate parameters affecting LAI and yield (i.e., TRIFL), as they contribute most of the uncertainty in the real-life case.

4. Discussion

4.1. *Uncertainty of the coupled model outputs*

The methodology implemented in this study was inspired by Moges et al. (2020), who investigated the uncertainty propagation of assimilated streamflow data on the parameters and outputs of a hydrological model and evaluated the relative contribution of the parameters and inputs to the overall model uncertainty. In contrast, the current study explored the uncertainty propagation of RS data in a coupled crop-radiative transfer model. Unlike a hydrological model, the period simulated by a crop model is restricted to the end of the growing season, and thus, improving the prediction accuracy early in the season is essential to enable practical decision support. Fig. 6 shows that in all the

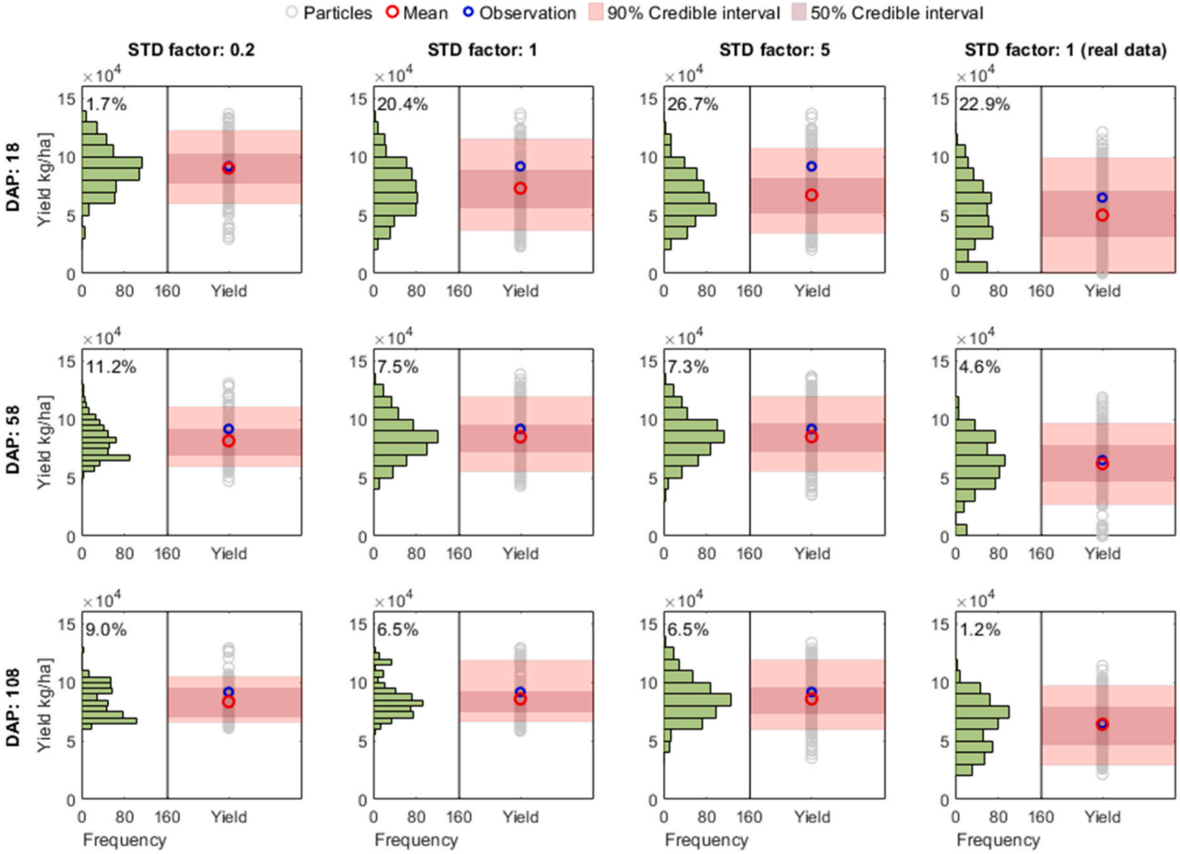

Fig. 6. – Final yield results of the particle filter for synthetic cases with three noise levels and the real-life case. The grey markers represent the particles, the red markers indicate the weighted mean of the final yield, and the blue markers represent the observed final yield. The light and dark red intervals represent the 90% and 50% credible intervals (CI), respectively. The number on the top-left corner of each subplot is the normalized absolute error between the observed final yield and the weighted mean. The histogram on the left side of each subplot shows the frequency of the yield values in the. Each row of subplots corresponds to a date on which DA was performed. The three leftmost columns present the synthetic cases with different noise levels, while the right column presents the real-life case.

presented cases, the yield NAE is equal to or smaller than 11.2 % and within the 50% CI at DAPs 58 and 108, which represent the middle and the end of the season, respectively. Conversely, Fig. 5 shows that for LAI, among the synthetic cases, only the one with an STD factor of 0.2 yielded a 50% CI that contained the observation. The LAI RMSE for the real-life case was comparable or higher relative to previous studies (Chen et al., 2022; Guo et al., 2019; Ntakos et al., 2024), and most of the measured values are within the 50% CI. The discrepancy between the yield and LAI results highlights that although LAI is highly influential on reflectance, the rest of the coupling relations are also essential in accounting for the crop state and predicting yield. Thus, assimilating only LAI might not be sufficient for successful yield prediction using a complex crop-radiative-transfer model.

An unexpected result shown in Fig. 6 is that at DAP 108, the synthetic case with an STD factor of 0.2 had larger 50% CI and RMSE values than the other two with higher noise levels. This finding is inconsistent with the results shown in Figs. 4 and 5, where for reflectance and LAI, at DAP 108, the RMSE values of the case with an STD factor of 0.2 were lower compared to the other two synthetic cases, and the 50% CI values were lower or comparable to the other two synthetic cases. The histograms in Fig. 6 at DAP 108 show that for the case with an STD factor of 0.2, the range of values is the smallest, but the distribution is more uniform compared to the other cases. A possible explanation for this surprising finding is the relatively poor convergence of the LFMAX parameter presented in Fig. 3. According to a sensitivity analysis presented by Weinman et al. (2025a), at the end of the season, LFMAX has a minor effect on the reflectance and LAI, while it still substantially affects yield. It can be hypothesized that due to the good convergence of the other parameters, the yield range of the 0.2 STD factor at DAP 108 is relatively low. Still, the variance in LFMAX leads to a variance of yield values within the small range, leading to a relatively high 50% CI and an inferior RMSE value.

4.2. Winding stairs analysis

Since the parameter distributions obtained by the PF (Fig. 3) were used for sampling during the WS procedure, they can explain the results presented in Figs. 7 and 8. That is, the larger values of BMV for the growth rate parameters are aligned with the higher values of the STD-range ratio values of the growth rate parameters in Fig. 3. This trend suggests that for the coupled model used here, calibrated with RS data, the higher contribution of the growth rate parameters to the total variance of simulated LAI and yield results from their poorer converge during the PF process.

Jansen et al. (1994) defined the BMV of a specific uncertainty source as the minimal residual variance one can achieve when all the other uncertainty sources become completely certain. Considering this definition, the results presented in Figs. 7 and 8 imply that, under the constraints of calibration with the RS data, the uncertainty related to the growth rate parameters accounts for most of the overall uncertainty. This finding is not encouraging since, compared to the phenology parameters, most growth rate parameters (e.g., LFMAX, XFRT, TRIFL) are more challenging to evaluate from field measurements. Hence, reducing the total uncertainty by improving the calibration of these growth rate parameters will require expanding the current coupling scheme or adding different observation types.

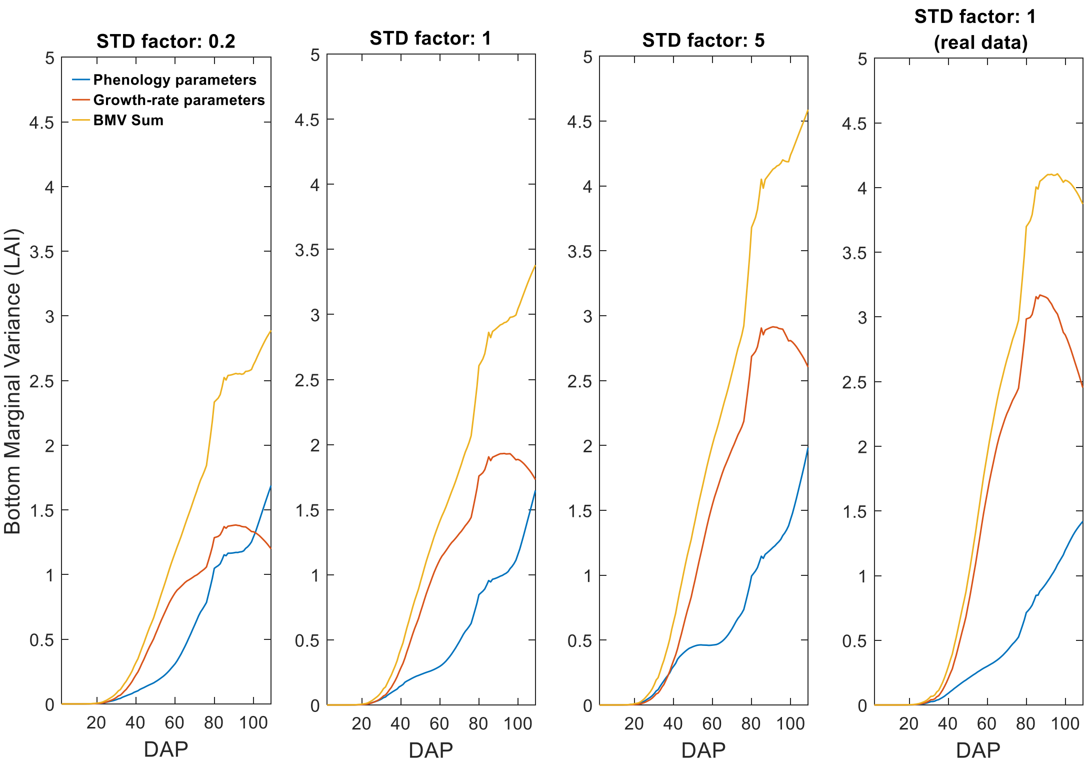

Fig. 7. –Bottom marginal variance (BMV) for LAI throughout the season for the synthetic cases with three noise levels and the real-life case. The blue curve shows the contribution of the phenology parameters to the total value of BMV, the orange curve shows the contribution of the growth rate parameters, and the yellow curve shows the sum of the blue and orange curves, indicating the total LAI variance associated with the examined parameters. The DSSAT's parameters used in the analysis are detailed in the legend.

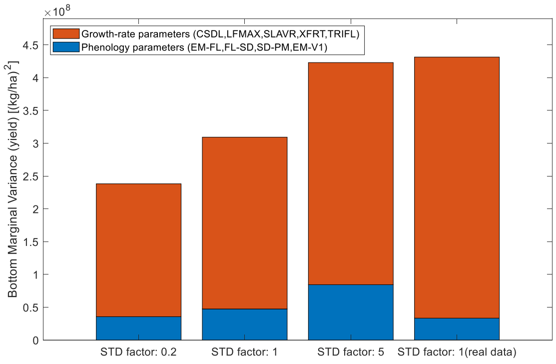

Fig. 8. Bottom marginal variance (BMV) for the final yield for the synthetic cases with three noise levels and the real-life case. The blue area shows the contribution of the phenology parameters to the total value of BMV, while the orange area shows the contribution of the non-phenological parameters. The DSSAT's parameters used in the analysis are detailed in the legend.

4.3. Shortcomings of the proposed method

A notable shortcoming of the uncertainty propagation method presented in this study is that it deals only with the uncertainty contributed by the model parameters within a calibrated model framework. In contrast, several studies showed that the contribution of other uncertainty sources (i.e., inputs, model structure) might be more substantial (e.g., Gao et al. (2021) and Ramirez-Villegas et al. (2017)). Restricting the analysis to the uncertainty contribution of the parameters stemmed from the inability to estimate the posterior distributions of the other uncertainty contributors, i.e., inputs and model structure, which would be required to include them in the WS analysis. The MC methods used for evaluating the parameters' posterior distributions under a given set of measurements do not determine the distributions of the model inputs. Moreover, when utilizing a model ensemble to evaluate the contribution of model structure uncertainty, it is challenging to decide which model is more reliable and, thus, should have more weight when averaging the ensemble results (Wallach et al., 2016). Even if one evaluates the distributions of all three uncertainty sources, using different, independent methods for each source would add a bias to the results stemming from the chosen methods rather than the model properties (Wallach et al., 2016). Moges et al. (2020) addressed this issue by examining two cases with different magnitudes of input uncertainty for a single input type (precipitation). The uncertainty levels were evaluated based on a literature review. However, this method is not general because it accounts for only two specific cases, and implementing it on several inputs (e.g., soil properties, weather, and management) will yield independent sets of results that cannot be compared. In summary, formulating an uncertainty propagation framework that will unbiasedly quantify the relative contributions of different uncertainty sources under a given set of measurements, while not all the sources are affected by the measurement noise, is a challenging task, requiring further investigation.

The ability of the uncertainty propagation analysis conducted in this study to represent real-life conditions appropriately is constrained since the reflectance noise was determined according to the spatial variance of the pixels within the experiment field (as was done by Machwitz et al. (2014)) rather than using a value derived from a physical approach. An optional source for assessing the reliability of Sentinel-2 products would be the Sentinel-2 level-2A uncertainty evaluation derived in Gorroño et al. (2023), who propagated the uncertainty induced by several factors (e.g., uncertainty in atmospheric parameters or Lambertian assumption error) to the total uncertainty of the top-of-the-canopy reflectance. However, Gorroño et al. (2023) found that the bands whose uncertainty is most affected by these factors are bands 1 (442 [nm]) and 9 (945 [nm]), which are particularly sensitive to atmospheric conditions. These bands were not used in this study as they are not informative for agronomic purposes. For most bands used here, the STD magnitude was similar to the scenarios examined by Gorroño et al. (2023).

5. Conclusions

This study investigated the uncertainty propagation of remote sensing data into a coupled crop-radiative-transfer model. The first step of this analysis was examining the results of a data assimilation procedure, which included the posterior distributions of the crop model parameters and the coupled model outputs, which consisted of reflectance, LAI, and yield. The analysis included running a DA procedure with synthetic data, including three levels of measurement noise, and with real-life data. The outcomes showed that the output uncertainties of the real-life and synthetic cases with the highest noise level (which had noise values five times higher) were comparable for most of the examined measures. This finding means that for the case presented here, the uncertainty sources of the model, stemming from model structure, parameters, and inputs, had a comparable effect on the total model uncertainty as increasing the assimilated data noise by a factor of five.

The next step was sampling from the parameter posterior distributions obtained by the particle filter to perform a winding stairs analysis. This investigation elucidated the contribution of model parameters to the total uncertainty of the coupled model under the constraint of the assimilated data. In this step, the parameters were separated into two groups - phenology and growth rate-related parameters - and the impact of each individual group was assessed. The results showed that, under the described DA, the growth rate-related parameters had a higher contribution to the overall uncertainty than the phenology-related parameters. This trend might be explained by the poorer convergence of the growth rate-related parameters during the PF process. These results indicate that improving the ability to estimate growth rate-related parameters using RS data with the suggested coupling scheme will reduce the uncertainty of the model predictions more than improving the calibration of the phenology parameters.

A limitation of the uncertainty analysis presented here is that it focused solely on the contribution of parameter uncertainty to the total output uncertainty. Since there are other uncertainty contributors, e.g., measurement noise, inputs, and model inaccuracies, future research should seek ways to compare the contribution of all uncertainty sources unbiasedly.

CRediT authorship contribution statement

Amit Weinman: Writing – original draft, Visualization, Validation, Software, Methodology, Investigation, Formal analysis, Data curation, Conceptualization. **Raphael Linker:** Writing – review & editing, Supervision, Project administration, Funding acquisition, Conceptualization. **Offer Rozenstein:** Writing – review & editing, Supervision, Project administration, Funding acquisition, Data curation, Conceptualization.

Software and data

The code for running the sensitivity-based particle filter with the real-life data from the 2019 season and the data from this season (used in this paper) is located at https://github.com/amitwn1/Particle-filter-coupled-model. This repository also contains a script for plotting the Particle Filter results. This code requires downloading DSSAT, available at https://dssat.net/main-download/, and SCOPE, available at https://github.com/Christiaanvandertol/SCOPE.

Declaration of competing interest

The authors declare the following financial interests/personal relationships which may be considered as potential competing interests: Offer Rozenstein reports financial support was provided by Agricultural Research Organization - Volcani Institute. If there are other authors, they declare that they have no known competing financial interests or personal relationships that could have appeared to influence the work reported in this paper.

Acknowledgments

This work was supported by the Chief Scientist of the Israel Ministry of Agriculture, Project 20-21-0010. In addition, the work received support from Action CA17134 SENSECO (Optical synergies for spatiotemporal sensing of scalable ecophysiological traits) and Action CA22136 PANGEOS (Pan-European Network of Green Deal Agriculture and Forestry Earth Observation Science) funded by COST (European Cooperation in Science and Technology, www.cost.eu (accessed on June 16, 2025). Amit Weinman received financial support from the Gerald Stanhill Scholarship fund of the Volcani International Partnerships.

Appendix A. – Names, descriptions, and values of the parameters used in the simulation run of the synthetic experiment

Table A1
– DSSAT-CROPGRO parameters adjusted during the particle filter with their names, descriptions, values used in the simulation run of the synthetic experiment, and ranges used in the data assimilation (particle filter)

Parameter name	Description	Range	The value used in the synthetic experiment
CSDL	Critical short-day Length below which reproductive development progresses with no day length effect (for short-day plants) [*hour*]	[10,15]	12.33
EM-FL	Time between plant emergence and flower appearance [*photothermal days*]	[16,28]	23.1
EM-V1	Time required from emergence to first true leaf [*thermal days*]	[10,30]	12
FL-SD	Time between first flower and first seed [*photothermal days*]	[9,25]	18.8
LFMAX	Maximum leaf photosynthesis rate at 30 $[^{\circ}C]$, 350 $[vpm]$ CO_2, and high light $\left[mg\ CO_2\ m^{-2}\ s^{-1}\right]$	[1.1,1.65]	1.5
RWDTH	Relative width of this ecotype in comparison to the standard width per node $[-]$	[0.8,1.2]	1
SD-PM	Time between first seed and physiological maturity [*photothermal days*]	[35,55]	45.2
SIZLF	Maximum size of full leaf (three leaflets) $\left[cm^2\right]$	[250,350]	320
SLAVR	Specific leaf area of cultivar under standard growth conditions $\left[cm^2\ g^{-1}\right]$	[300,410]	375
TRIFL	Rate of appearance of leaves on the mainstem [*leaves per photothermal days*]	[0.25,0.6]	0.35
XFRT	Maximum fraction of daily growth that is partitioned to seed + shell $[-]$	[0.55.0.8]	0.8

Table A2

– DSSAT-CROPGRO parameters not adjusted during the particle filer with their names, descriptions, and values used in the simulation run of the synthetic experiment

Parameter name	Description	The value used in the synthetic experiment
FL-LF	Time between first flower and end of leaf expansion [*photothermal days*]	51.35
FL-SH	Time between first flower and first pod [*photothermal days*]	3
FL-VS	Time from first flower to last leaf on main stem [*photothermal days*]	24.5
JU-R0	Time required for floral induction, equal to the minimum number of days for floral induction under optimal temperature and daylengths [*photothermal days*]	5
LNGSH	Time required for growth of individual shells [*photothermal days*]	39
PM09	Portion of time between first seed and physiological maturity that the last seed can be formed [−]	0.75
PODUR	Time required for cultivar to reach final pod load under optimal conditions [*photothermal days*]	58
PPSEN	Slope of the relative response of development to photoperiod with time $[hour^{-1}]$	0
R7-R8	Time between physiological and harvest maturity [*days*]	0
THVAR	Minimum rate of reproductive development under short days and optimal temperature [−]	0
V1-JU	Time required from first true leaf to end of juvenile phase [*thermal days*]	0

Appendix B. – Sentinel-2 bands used in data assimilation

Table B1

– Properties of Sentinel-2 bands used in this research

Band	Sentinel-2A		Sentinel-2B		Spatial resolution [m]
	Central wavelength [nm]	Bandwidth [nm]	Central wavelength [nm]	Bandwidth [nm]	
B2 - Blue	492.4	66	492.1	66	10
B3 - Green	559.8	36	559.0	36	10
B4 - Red	664.6	31	664.9	31	10
B5 - Red edge	704.1	15	703.8	16	20
B6 - Red edge	740.5	15	739.1	15	20
B7 - Red edge	782.8	20	779.7	20	20
B9 - Narrow NIR	864.7	21	864.0	22	20
B12 - SWIR	1613.7	91	1610.4	94	20
B13 - SWIR	2202.4	175	2185.7	185	20

Data availability

Data will be made available on request.

References

Alderman, P.D., Stanfill, B., 2017. Quantifying Model-Structure- and parameter-driven uncertainties in spring wheat phenology prediction with bayesian analysis. Eur. J. Agron. 88, 1–9. https://doi.org/10.1016/j.eja.2016.09.016.

Asseng, S., Zhu, Y., Wang, E., Zhang, W., 2015. Crop modeling for climate change impact and adaptation. In: Crop Physiology. Elsevier, pp. 505–546. https://doi.org/10.1016/B978-0-12-417104-6.00020-0.

Boote, K.J., Sau, F., Hoogenboom, G., Jones, J.W., 2008. Experience with water balance, evapotranspiration, and predictions of water stress effects in the CROPGRO model. In: Ahuja, L.R., Reddy, V.R., Saseendran, S.A., Yu, Q. (Eds.), Advances in Agricultural Systems Modeling. American Society of Agronomy and Soil Science Society of America, Madison, WI, USA, pp. 59–103. https://doi.org/10.2134/advagricsystmodel1.c3.

Bosi, C., Sentelhas, P.C., Pezzopane, J.R.M., Santos, P.M., 2020. CROPGRO-perennial forage model parameterization for simulating Piatã palisade grass growth in monoculture and in a silvopastoral system. Agric. Syst. 177, 102724. https://doi.org/10.1016/j.agsy.2019.102724.

Cammarano, D., Ronga, D., Di Mola, I., Mori, M., Parisi, M., 2020. Impact of climate change on water and nitrogen use efficiencies of processing tomato cultivated in Italy. Agric. Water Manag. 241, 106336. https://doi.org/10.1016/j.agwat.2020.106336.

Chan, K., Saltelli, A., Tarantola, S., 2000. Winding stairs: a sampling tool to compute sensitivity indices. Stat. Comput. 10, 187–196. https://doi.org/10.1023/A:1008950625967.

Chapagain, R., Remenyi, T.A., Harris, R.M.B., Mohammed, C.L., Huth, N., Wallach, D., Rezaei, E.E., Ojeda, J.J., 2022. Decomposing crop model uncertainty: a systematic review. Field Crops Res. 279, 108448. https://doi.org/10.1016/j.fcr.2022.108448.

Chen, Q., Zheng, B., Chen, T., Chapman, S.C., 2022. Integrating a crop growth model and radiative transfer model to improve estimation of crop traits based on deep learning. J. Exp. Bot. 73, 6558–6574. https://doi.org/10.1093/jxb/erac291.

Correndo, A.A., Tremblay, N., Coulter, J.A., Ruiz-Diaz, D., Franzen, D., Nafziger, E., Prasad, V., Rosso, L.H.M., Steinke, K., Du, J., Messina, C.D., Ciampitti, I.A., 2021. Unraveling uncertainty drivers of the maize yield response to nitrogen: a bayesian and machine learning approach. Agric. For. Meteorol. 311, 108668. https://doi.org/10.1016/j.agrformet.2021.108668.

Dan, Y., Raz, T., 1970. Israel Soil Groups, 250.

de Wit, A., Boogaard, H., Fumagalli, D., Janssen, S., Knapen, R., van Kraalingen, D., Supit, I., van der Wijngaart, R., van Diepen, K., 2019. 25 years of the WOFOST cropping systems model. Agric. Syst. 168, 154–167. https://doi.org/10.1016/j.agsy.2018.06.018.

Dlamini, L., Crespo, O., Van Dam, J., Kooistra, L., 2023. A global systematic review of improving crop model estimations by assimilating remote sensing data: implications for small-scale agricultural systems. Remote Sens. 15, 4066. https://doi.org/10.3390/rs15164066.

Ellison, A.M., 2004. Bayesian inference in ecology. Ecol. Lett. 7, 509–520. https://doi.org/10.1111/j.1461-0248.2004.00603.x.

Gao, Y., Wallach, D., Hasegawa, T., Tang, L., Zhang, R., Asseng, S., Kahveci, T., Liu, L., He, J., Hoogenboom, G., 2021. Evaluation of crop model prediction and uncertainty using Bayesian parameter estimation and Bayesian model averaging. Agric. For. Meteorol. 311, 108686. https://doi.org/10.1016/j.agrformet.2021.108686.

García-Haro, F.J., Campos-Taberner, M., Muñoz-Marí, J., Laparra, V., Camacho, F., Sánchez-Zapero, J., Camps-Valls, G., 2018. Derivation of global vegetation biophysical parameters from EUMETSAT polar system. ISPRS J. Photogrammetry Remote Sens. 139, 57–74. https://doi.org/10.1016/j.isprsjprs.2018.03.005.

Ghorbani, K., Salarijazi, M., Bararkhanpour, S., Ghaleh, L.R., 2023. Comparison of Bayesian and frequentist quantile regressions in studying the trend of discharge changes in several hydrometric stations of the Gorganroud basin in Iran. J. Water Clim. Change 14, 3753–3769. https://doi.org/10.2166/wcc.2023.305.

Gorroño, J., Fomferra, N., Peters, M., Gascon, F., Underwood, C., Fox, N., Kirches, G., Brockmann, C., 2017. A radiometric uncertainty tool for the sentinel 2 mission. Remote Sens. 9, 178. https://doi.org/10.3390/rs9020178.

Gorroño, J., Guanter, L., Graf, L.V., Gascon, F., 2023. A software tool for the estimation of uncertainties and spectral error correlation in Sentinel-2 Level-2A data products. https://doi.org/10.31223/X5GM33.

Graf, L.V., Gorroño, J., Hueni, A., Walter, A., Aasen, H., 2023. Propagating Sentinel-2 top-of-atmosphere radiometric uncertainty into land surface phenology metrics using a monte carlo framework. IEEE J. Sel. Top. Appl. Earth Obs. Rem. Sens. 16, 8632–8654. https://doi.org/10.1109/JSTARS.2023.3297713.

Guler, S., Buyuk, G., 2007. Relationships among Chlorophyl-Meter reading value, leaf N and yield of cucumber and tomatoes. In: Acta Horticulturae. International Society for Horticultural Science (ISHS), Leuven, Belgium, pp. 307–311. https://doi.org/10.17660/ActaHortic.2007.729.50.

Guo, C., Tang, Y., Lu, J., Zhu, Y., Cao, W., Cheng, T., Zhang, L., Tian, Y., 2019. Predicting wheat productivity: integrating time series of vegetation indices into crop modeling via sequential assimilation. Agric. For. Meteorol. 272–273, 69–80. https://doi.org/10.1016/j.agrformet.2019.01.023.

Huang, J., Gómez-Dans, J.L., Huang, H., Ma, H., Wu, Q., Lewis, P.E., Liang, S., Chen, Z., Xue, J.-H., Wu, Y., Zhao, F., Wang, J., Xie, X., 2019a. Assimilation of remote sensing into crop growth models: current status and perspectives. Agric. For. Meteorol., 107609 https://doi.org/10.1016/j.agrformet.2019.06.008, 276–277.

Huang, J., Ma, H., Sedano, F., Lewis, P., Liang, S., Wu, Q., Su, W., Zhang, X., Zhu, D., 2019b. Evaluation of regional estimates of winter wheat yield by assimilating three remotely sensed reflectance datasets into the coupled WOFOST–PROSAIL model. Eur. J. Agron. 102, 1–13. https://doi.org/10.1016/j.eja.2018.10.008.

Huang, J., Song, J., Huang, H., Zhuo, W., Niu, Q., Wu, S., Ma, H., Liang, S., 2024. Progress and perspectives in data assimilation algorithms for remote sensing and crop growth model. Science of Remote Sensing 10, 100146. https://doi.org/10.1016/j.srs.2024.100146.

Jacquemoud, S., Baret, F., 1990. PROSPECT: a model of leaf optical properties spectra. Rem. Sens. Environ. 34, 75–91. https://doi.org/10.1016/0034-4257(90)90100-Z.

Jamal, A., Linker, R., 2020. Genetic operator-based particle filter combined with Markov chain Monte Carlo for data assimilation in a crop growth model. Agriculture 10, 606. https://doi.org/10.3390/agriculture10120606.

Jansen, M.J.W., Rossing, W.A.H., Daamen, R.A., 1994. Monte Carlo estimation of uncertainty contributions from several independent multivariate sources. In: Grasman, J., Van Straten, G. (Eds.), Predictability and Nonlinear Modelling in Natural Sciences and Economics. Springer, Netherlands, Dordrecht, pp. 334–343. https://doi.org/10.1007/978-94-011-0962-8_28.

Jiang, C., Johkan, M., Hohjo, M., Tsukagoshi, S., Maturo, T., 2017. A correlation analysis on chlorophyll content and SPAD value in tomato leaves. Hortscience 71, 37–42.

Jin, X., Kumar, L., Li, Z., Feng, H., Xu, X., Yang, G., Wang, J., 2018. A review of data assimilation of remote sensing and crop models. Eur. J. Agron. 92, 141–152. https://doi.org/10.1016/j.eja.2017.11.002.

Jones, J.W., Dayan, E., Allen, L.H., Van Keulen, H., Challa, H., 1991. A dynamic tomato growth and yield model (TOMGRO). Transactions of the ASAE 34, 663–672. https://doi.org/10.13031/2013.31715.

Jones, J.W., Hoogenboom, G., Boote, K.J., Porter, C.H., 2010. DSSAT v4.5 cropping system model documentation. DSSAT v4.5: Crop Model Documentation. University of Hawaii, Honolulu, HI.

Jones, J.W., Hoogenboom, G., Porter, C.H., Boote, K.J., Batchelor, W.D., Hunt, L.A., Wilkens, P.W., Singh, U., Gijsman, A.J., Ritchie, J.T., 2003. The DSSAT cropping system model. Eur. J. Agron. 18, 235–265. https://doi.org/10.1016/S1161-0301(02)00107-7.

Kaplan, G., Fine, L., Lukyanov, V., Manivasagam, V.S., Malachy, N., Tanny, J., Rozenstein, O., 2021. Estimating processing tomato water consumption, leaf area index, and height using Sentinel-2 and VENμS imagery. Remote Sens. 13, 1046. https://doi.org/10.3390/rs13061046.

King, R., Sarzo, B., Elvira, V., 2023. When ecological individual heterogeneity models and large data collide: an importance sampling approach. Ann. Appl. Stat. 17. https://doi.org/10.1214/23-AOAS1753.

Levitan, N., Kang, Y., Özdoğan, M., Magliulo, V., Castillo, P., Moshary, F., Gross, B., 2019. Evaluation of the uncertainty in satellite-based crop state variable retrievals due to site and growth stage specific factors and their potential in coupling with crop growth models. Remote Sens. 11, 1928. https://doi.org/10.3390/rs11161928.

Lin, C., Yang, Y.E., 2022. The effects of model complexity on model output uncertainty in co-evolved coupled natural-human systems. Earths Future 10, e2021EF002403. https://doi.org/10.1029/2021EF002403.

Machwitz, M., Giustarini, L., Bossung, C., Frantz, D., Schlerf, M., Lilienthal, H., Wandera, L., Matgen, P., Hoffmann, L., Udelhoven, T., 2014. Enhanced biomass prediction by assimilating satellite data into a crop growth model. Environ. Model. Software 62, 437–453. https://doi.org/10.1016/j.envsoft.2014.08.010.

Milner-Gulland, E.J., Shea, K., 2017. Embracing uncertainty in applied ecology. J. Appl. Ecol. 54, 2063–2068. https://doi.org/10.1111/1365-2664.12887.

Moges, E., Demissie, Y., Li, H., 2020. Uncertainty propagation in coupled hydrological models using winding stairs and null-space Monte carlo methods. J. Hydrol. 589, 125341. https://doi.org/10.1016/j.jhydrol.2020.125341.

Ntakos, G., Prikaziuk, E., Ten Den, T., Reidsma, P., Vilfan, N., Van Der Wal, T., Van Der Tol, C., 2024. Coupled wofost and SCOPE model for remote sensing-based crop growth simulations. Comput. Electron. Agric. 225, 109238. https://doi.org/10.1016/j.compag.2024.109238.

Omlin, M., Reichert, P., 1999. A comparison of techniques for the estimation of model prediction uncertainty. Ecol. Model. 115, 45–59. https://doi.org/10.1016/S0304-3800(98)00174-4.

Orlova, Y., Linker, R., 2023. Data assimilation with sensitivity-based particle filter: a simulation study with AquaCrop. Comput. Electron. Agric. 204, 107538. https://doi.org/10.1016/j.compag.2022.107538.

Ramirez-Villegas, J., Koehler, A.-K., Challinor, A.J., 2017. Assessing uncertainty and complexity in regional-scale crop model simulations. Eur. J. Agron. 88, 84–95. https://doi.org/10.1016/j.eja.2015.11.021.

Ran, H., Kang, S., Hu, X., Yao, N., Li, S., Wang, W., Galdos, M.V., Challinor, A.J., 2022. A framework to quantify uncertainty of crop model parameters and its application in arid Northwest China. Agric. For. Meteorol. 316, 108844. https://doi.org/10.1016/j.agrformet.2022.108844.

Rosenzweig, C., Jones, J.W., Hatfield, J.L., Ruane, A.C., Boote, K.J., Thorburn, P., Antle, J.M., Nelson, G.C., Porter, C., Janssen, S., Asseng, S., Basso, B., Ewert, F., Wallach, D., Baigorria, G., Winter, J.M., 2013. The agricultural model intercomparison and improvement project (AgMIP): Protocols and pilot studies. Agric. For. Meteorol. 170, 166–182. https://doi.org/10.1016/j.agrformet.2012.09.011.

Scholberg, J.M.S., Boote, K.J., Jones, J.W., McNeal, B.L., 1997. Adaptation of the CGROPGRO model to simulate the growth of field-grown tomato. In: Kropff, M.J., Teng, P.S., Aggarwal, P.K., Bouma, J., Bouman, B.A.M., Jones, J.W., Van Laar, H.H. (Eds.), Applications of Systems Approaches at the Field Level, Systems Approaches for Sustainable Agricultural Development. Springer, Netherlands, Dordrecht, pp. 135–151. https://doi.org/10.1007/978-94-017-0754-1_9.

Senatore, A., Fuoco, D., Maiolo, M., Mendicino, G., Smiatek, G., Kunstmann, H., 2022. Evaluating the uncertainty of climate model structure and bias correction on the hydrological impact of projected climate change in a Mediterranean catchment. J. Hydrol.: Reg. Stud. 42, 101120. https://doi.org/10.1016/j.ejrh.2022.101120.

Teixeira, E.I., Zhao, G., Ruiter, J.D., Brown, H., Ausseil, A.-G., Meenken, E., Ewert, F., 2017. The interactions between genotype, management and environment in regional crop modelling. Eur. J. Agron. 88, 106–115. https://doi.org/10.1016/j.eja.2016.05.005.

Uusitalo, L., Lehikoinen, A., Helle, I., Myrberg, K., 2015. An overview of methods to evaluate uncertainty of deterministic models in decision support. Environ. Model. Software 63, 24–31. https://doi.org/10.1016/j.envsoft.2014.09.017.

van der Tol, C., Rossini, M., Cogliati, S., Verhoef, W., Colombo, R., Rascher, U., Mohammed, G., 2016. A model and measurement comparison of diurnal cycles of sun-induced chlorophyll fluorescence of crops. Rem. Sens. Environ. 186, 663–677. https://doi.org/10.1016/j.rse.2016.09.021.

Van Griensven, A., Meixner, T., Grunwald, S., Bishop, T., Diluzio, M., Srinivasan, R., 2006. A global sensitivity analysis tool for the parameters of multi-variable catchment models. J. Hydrol. 324, 10–23. https://doi.org/10.1016/j.jhydrol.2005.09.008.

Van Leeuwen, P.J., 2009. Particle filtering in geophysical systems. Mon. Weather Rev. 137 (1), 4089–4114. https://doi.org/10.1175/2009MWR2835.

Verhoef, W., 1984. Light scattering by leaf layers with application to canopy reflectance modeling: the SAIL model. Rem. Sens. Environ. 16, 125–141. https://doi.org/10.1016/0034-4257(84)90057-9.

Verhoef, W., Van Der Tol, C., Middleton, E.M., 2018. Hyperspectral radiative transfer modeling to explore the combined retrieval of biophysical parameters and canopy fluorescence from FLEX – sentinel-3 Tandem mission multi-sensor data. Rem. Sens. Environ. 204, 942–963. https://doi.org/10.1016/j.rse.2017.08.006.

Wallach, D., Keussayan, N., Brun, F., Lacroix, B., Bergez, J.-E., 2012. Assessing the uncertainty when using a model to compare irrigation strategies. Agron. J. 104, 1274–1283. https://doi.org/10.2134/agronj2012.0038.

Wallach, D., Thorburn, P., Asseng, S., Challinor, A.J., Ewert, F., Jones, J.W., Rotter, R., Ruane, A., 2016. Estimating model prediction error: should you treat predictions as fixed or random? Environ. Model. Software 84, 529–539. https://doi.org/10.1016/j.envsoft.2016.07.010.

Wallach, D., Thorburn, P.J., 2017. Estimating uncertainty in crop model predictions: current situation and future prospects. Eur. J. Agron. 88, A1–A7. https://doi.org/10.1016/j.eja.2017.06.001.

Walther, F., Barton, D.N., Schwaab, J., Kato-Huerta, J., Immerzeel, B., Adamescu, M., Andersen, E., Arámbula Coyote, M.V., Arany, I., Balzan, M., Bruggeman, A., Carvalho-Santos, C., Cazacu, C., Geneletti, D., Giuca, R., Inácio, M., Lagabrielle, E., Lange, S., Clec’h, S.L., Vanessa Lim, Z.Y., Mörtberg, U., Nedkov, S., Portela, A.P., Porucznik, A., Racoviceanu, T., Rendón, P., Ribeiro, D., Seguin, J., Hribar, M.Š., Stoycheva, V., Vejre, H., Zoumides, C., Grêt-Regamey, A., 2025. Uncertainties in ecosystem services assessments and their implications for decision support – a semi-systematic literature review. Ecosyst. Serv. 73, 101714. https://doi.org/10.1016/j.ecoser.2025.101714.

Weinman, A., Linker, R., Rozenstein, O., 2025a. Investigation of coupling DSSAT with SCOPE-RTMo via sensitivity analysis and use of this coupled crop-radiative transfer model for sensitivity-based data assimilation. Eur. J. Agron. 162, 127431. https://doi.org/10.1016/j.eja.2024.127431.

Weinman, A., Malachy, N., Linker, R., Rozenstein, O., 2025b. Assimilation of UAV multispectral imagery into a coupled DSSAT-CROPGRO – SCOPE model for processing tomatoes. Comput. Electron. Agric. 236, 110460. https://doi.org/10.1016/j.compag.2025.110460.

Weiss, M., Baret, F., 2016. S2ToolBox Level 2 Products: LAI, FAPAR, FCOVER.

Weksler, S., Rozenstein, O., Ben Dor, E., 2022. Continuous seasonal monitoring of nitrogen and water content in lettuce using a dual phenomics system. J. Exp. Bot. 73, 5294–5305. https://doi.org/10.1093/jxb/erab561.

White, J.T., Fienen, M.N., Doherty, J.E., 2016. A python framework for environmental model uncertainty analysis. Environ. Model. Software 85, 217–228. https://doi.org/10.1016/j.envsoft.2016.08.017.

Wilkens, P.W., Hoogenboom, G., Jones, J.W., Porter, C.H., Uryasev, O., 2010. DSSAT v4.5 cropping system model documentation - volume 2., DSSAT v4.5. Crop Model Documentation. University of Hawaii, Honolulu, HI.

Xu, M., Wang, C., Ling, L., Batchelor, W.D., Zhang, J., Kuai, J., 2021. Sensitivity analysis of the CROPGRO-canola model in China: a case study for rapeseed. PLoS One 16, e0259929. https://doi.org/10.1371/journal.pone.0259929.

Yang, P., Prikaziuk, E., Verhoef, W., van der Tol, C., 2020. Scope 2.0: a model to simulate vegetated land surface fluxes and satellite signals. Biogeosciences. https://doi.org/10.5194/gmd-2020-251.

Yang, P., Van Der Tol, C., Verhoef, W., Damm, A., Schickling, A., Kraska, T., Muller, O., Rascher, U., 2019. Using reflectance to explain vegetation biochemical and structural effects on sun-induced chlorophyll fluorescence. Rem. Sens. Environ. 231, 110996. https://doi.org/10.1016/j.rse.2018.11.039.

Zare, H., Weber, T.K.D., Ingwersen, J., Nowak, W., Gayler, S., Streck, T., 2022. Combining crop modeling with remote sensing data using a particle filtering technique to produce real-time forecasts of winter wheat yields under uncertain boundary conditions. Remote Sens. 14, 1360. https://doi.org/10.3390/rs14061360.

Zheng, Z., Zhao, L., Oleson, K.W., 2021. Large model structural uncertainty in global projections of urban heat waves. Nat. Commun. 12, 3736. https://doi.org/10.1038/s41467-021-24113-9.